agronomy

MDPI

*Article*

# Defining the Ideal Phenological Stage for Estimating Corn Yield Using Multispectral Images

**Carlos Alberto Matias de Abreu Júnior [1], George Deroco Martins [1], Laura Cristina Moura Xavier [1,*], João Vitor Meza Bravo [2], Douglas José Marques [1] and Guilherme de Oliveira [3]**

[1] Institute of Agrarian Sciences, Federal University of Uberlândia, Monte Carmelo 38500-000, Brazil; carlosalberto0103@hotmail.com (C.A.M.d.A.J.); deroco@ufu.br (G.D.M.); douglas.marques@ufu.br (D.J.M.)
[2] Institute of Geography, Federal University of Uberlândia, Monte Carmelo 38500-000, Brazil; jvmbravo@ufu.br
[3] Lallemand Soluções Biológicas LTDA, Patos de Minas 38706-420, Brazil; goliveira@lallemand.com
* Correspondence: xavier.lauramoura@gmail.com; Tel.: +55-34-3810-1042

**Abstract:** Image-based spectral models assist in estimating the yield of maize. During the vegetative and reproductive phenological phases, the corn crop undergoes changes caused by biotic and abiotic stresses. These variations can be quantified using spectral models, which are tools that help producers to manage crops. However, defining the correct time to obtain these images remains a challenge. In this study, the possibility to estimate corn yield using multispectral images is hypothesized, while considering the optimal timing for detecting the differences caused by various phenological stages. Thus, the main objective of this work was to define the ideal phenological stage for taking multispectral images to estimate corn yield. Multispectral bands and vegetation indices derived from the Planet satellite were considered as predictor variables for the input data of the models. We used root mean square error percentage and mean absolute percentage error to evaluate the accuracy and trend of the yield estimates. The reproductive phenological phase R2 was found to be optimal for determining the spectral models based on the images, which obtained the best root mean square error percentage of 9.17% and the second-best mean absolute percentage error of 7.07%. Here, we demonstrate that it is possible to estimate yield in a corn plantation in a stage before the harvest through Planet multispectral satellite images.

**Keywords:** corn phenological stages; remote monitoring; yield prediction; spatial distribution of yield

check for updates

**Citation:** Abreu Júnior, C.A.M.d.; Martins, G.D.; Xavier, L.C.M.; Bravo, J.V.M.; Marques, D.J.; Oliveira, G.d. Defining the Ideal Phenological Stage for Estimating Corn Yield Using Multispectral Images. *Agronomy* **2023**, *13*, 2390. https://doi.org/10.3390/agronomy13092390

Academic Editors: Yanbo Huang, Xin Zhang and Chandan Kumar

Received: 2 August 2023
Revised: 5 September 2023
Accepted: 6 September 2023
Published: 15 September 2023

**Copyright:** © 2023 by the authors. Licensee MDPI, Basel, Switzerland. This article is an open access article distributed under the terms and conditions of the Creative Commons Attribution (CC BY) license (https://creativecommons.org/licenses/by/4.0/).

## 1. Introduction

Estimating yield is a critical agronomic parameter for assisting the national and international market in terms of demand, transport capacity, and storage of agricultural products. It is possible to commercialize and ascertain prices by predicting crop yields and considering the quantity of product that will be generated prior to the harvest [1].

Yield can be estimated by combining the collection of biophysical parameters sampled in the field [2] and the information obtained using remote sensing techniques [3]. These techniques consist of analyzing the spectral response of crops and the targets present on the surface, which are obtained with multispectral sensors attached to satellites, remotely piloted aircrafts, or field machinery [4]. A critical aspect of yield mapping is that it can detect areas with lower yield potential, which may eventually be associated with nutritional deficiencies of the plants or soil.

Multispectral images that are used to estimate yield follow scientific methodologies [5]. However, determining the period at which images should be obtained, the definition of spectral bands, and the ideal vegetation indices for constructing prediction models that are conditioned to the spectral characteristics of the different phenological stages of crops, remains a challenge [6]. This occurs because each crop has agricultural variations, including the type of management required for the structural changes inherent to each type of crop,

such as the time of cultivation [7]. For example, annual and perennial crops exhibit distinct phenological stages and different spectral responses, and their conditions are influenced by canopy geometry, biomass, leaf area index, and leaf senescence [7]. Specifically, during the vegetative and reproductive phases, the maize crop experiences stress that can reduce yield. Depending on the moment of image acquisition for stress detection, it is uncertain whether the spectral responses detect the condition affecting a plant, especially when using a limited data set; thus, yield mapping becomes unfeasible.

In recent studies, spectral models for yield estimation based on machine learning and MODIS [8], Landsat 8 [9], and aerial [10] showed greater accuracy with the use of images obtained in the phenological stage, called the reproductive phase (R2 and R3), that is, the period that varies from 12 to 18 days after the fertilization when the culture presents a significant gain in biomass. However, these models are often developed in the late stage and do not precisely estimate the absolute value of yield; decades of agricultural remote sensing studies indicate that for any crop, the spectral bands always have a high sensitivity to agronomic parameters that correlate with the production factors, making them potential predictor variables.

Based on the aforementioned findings, in this study, we assume that the actual contribution of spectral models for estimating yield is related to how useful they are for management practices of maize crops, in addition to the potential accuracy of the absolute value of production. The application of the current spectral models for yield prediction [11,12] have limitations owing to the fact that these methodologies [13] only recommend estimations at advanced phenological stages of maize development, that is, stages in which interventions in the crop will only make a slight difference in the final yield [11].

Therefore, given the hypothesis that it is possible to estimate the yield of corn using multispectral orbital images and algorithms based on machine learning, the objective of this study was to evaluate whether there is an ideal phenological stage that accurately estimates yield in a timely manner for applying management practices that will increase the productive potential of the crop. The accuracy of multispectral prediction models based on machine learning algorithms (neural networks, support vector machines, random forests, and decision trees) was evaluated from the surface reflectance extracted from Planet images that was obtained during the main phenological stages of a corn crop.

It is worth emphasizing that our research presents a solution for precision agriculture and decision-making in the agricultural management of corn. Even at the predicted stages of ear reproduction, the spectral estimation models showed the possibility of an accurate large-scale monitoring of yield in commercial plots. Therefore, the advantages of using the models presented are as follows:

- Possibility of remote monitoring of yield;
- Prediction of places of high and low productivity in the first reproductive stages of maize;
- Provision of a database on culture within the scope of digital agriculture;
- Mapping of the geospatial distribution of crop production for later decision-making.

Finally, this work presents a possibility of monitoring with the exclusive use of remote data, as opposed to the current spectral models, which are mostly hybrids.

## 2. Materials and Methods

### *2.1. Areas of Study*

This study was conducted in the municipality of Patos de Minas, which is in the mesoregion of Triângulo Mineiro and Alto Paranaíba, Minas Gerais, Brazil (Figure 1). The study area (21.56 ha) has red latosol, an average altitude of 938 m, consists of flat and wavy relief, and has an average annual precipitation of 950 mm. The mesoregion of Triângulo Mineiro and Alto Paranaíba is one of the main producers of grains in the state of Minas Gerais, Brazil. The high production is attributed to corn and soybean crops owing to the high technological development of this region [14]. Temperature is a driving factor of this production [15]; according to [16], the mesoregion of Triângulo Mineiro and Alto Paranaíba,

Brazil has a tropical climate with mild and dry winter seasons. The average temperatures in the region vary from 23 °C to 28 °C during summer, and from 16 °C to 21 °C during winter. These temperatures tend to be favorable for the development of the second crop corn [14].

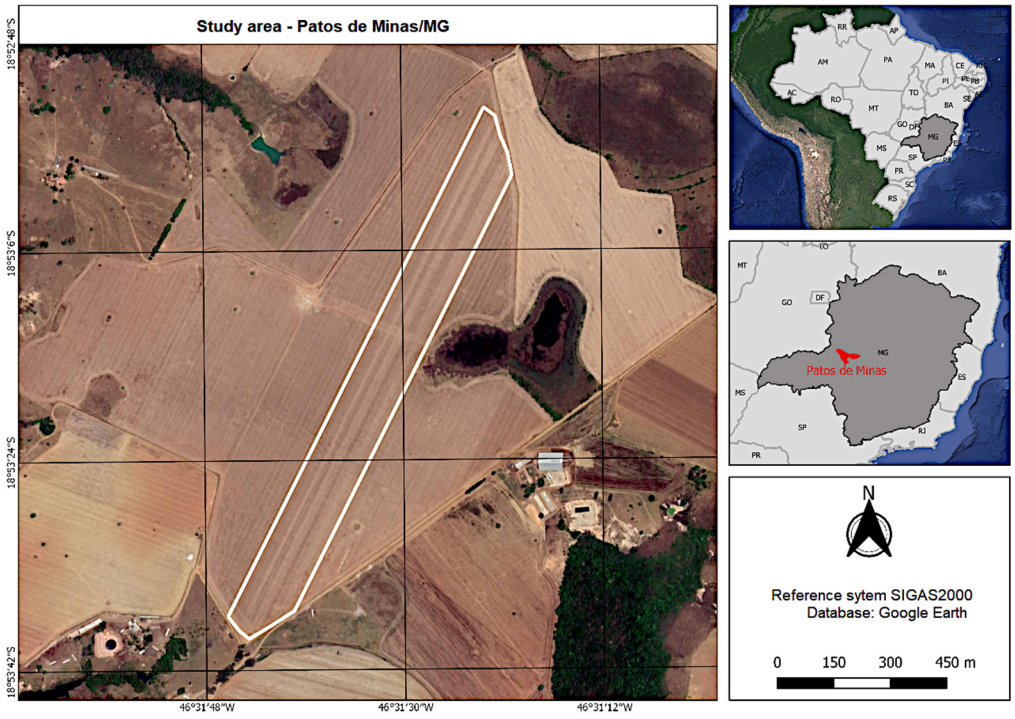


**Figure 1.** Area used for this study: the municipality of Patos de Minas, Minas Gerais State, Brazil.

### *2.2. The Methodology Used for Data Processing*

The estimation models and their respective predictor variables, namely, the image bands and multispectral indices, the regression algorithms (machine learning), and the estimated variable (yield) were based on [17,18]. In general, the methodology presented in Figure 2 was developed considering the following stages: data acquisition of yield, obtaining images during various phenological stages, defining algorithms for yield estimation, method validation, and mapping the yield spatial distribution. Thus, the research steps are defined as follows: (I) data acquisition, (II) pre-processing, (III) data sampling and filtering, (IV) generation of prediction models, (V) validation of the accuracy of the models, and (VI) confection of thematic maps.

### *2.3. Delimitation of the Experiment*

To analyze the yield data, the study area was standardized in the municipality of Patos de Minas (Figure 1). The harvests were performed on 8 August 2020, during the second crop period, considering the national market of the crop in Brazil. The experiment was set up using an inter-row spacing of 0.5 m with a distribution of 3 plants per meter. Thus, the vertical spacing was approximately 0.33 m. Twenty-four lines were arranged in an irregular polygon with an area equal to 21.56 ha. The AG8088 PRO2 corn cultivator was used. A harvester index, New Holland CR 9060 model, was considered for the estimation of yield. For data of this nature, the yield is presented in tons per hectare in a spacing of one $m^2$. The files are available in a georeferenced vector format (shapefile).

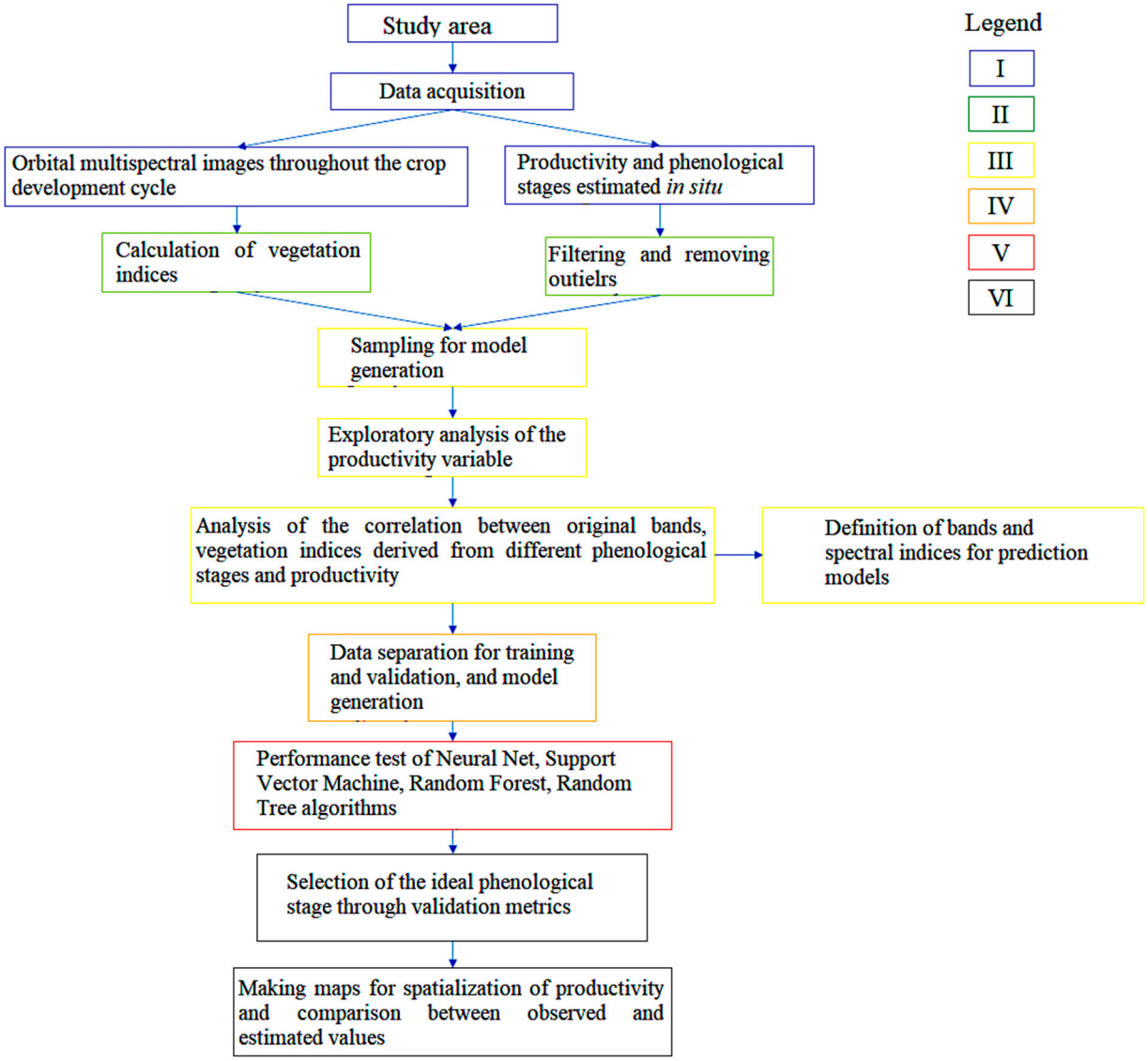


**Figure 2.** Methodological flowchart used in research. Blue boxes: data acquisition and filtering; yellow boxes: data pre-processing; pink box: generation of prediction models; black box: validation of results.

### *2.4. Filtering of Maize Crop Yield Data*

For treatment and filtering of the yield data, we defined the following two sample removal criteria: (1) definition of a confidence interval to remove outliers, and (2) removal of noise from the automated harvesting process. (1) We define the confidence interval as recommended based on 151 classical statistics for removing outliers; that is, we remove any outlier measurement from a sample set given by the condition $\mu \pm 3 \times \sigma$, where $\mu$ is the mean of the yield data, and $\sigma$ is the standard deviation of the yield data. Thus, we established the upper and lower thresholds based on the population mean, defining a confidence interval of 99.7%. (2) We excluded the noises as recommended by the manual of the harvester manufacturers; that is, null data and those indicating negative yield were eliminated from the samples. In Equation (1), the lower values have a minimum threshold of zero because it is not possible to assign negative yield to plants to exclude outliers. Thus, values not belonging to the interval were excluded.

### *2.5. Descriptive and Exploratory Analysis of Yield*

We performed a descriptive analysis of the yield data for a detailed description of the production of each area. We calculated the mean, standard deviation, and coefficient of variation for this variable. Furthermore, an exploratory analysis was also performed, in which the values of the maximum, minimum, quartile 1, quartile 2, median, and histogram of the variables were estimated.

### *2.6. Acquisition of Multispectral Data*

Yield estimation models using multispectral images of high spatial resolution are widely applied in studies for short-cycle crops because they enable visualization of the spatial distribution of the more and less productive areas. The images that comprise the purely spectral models are captured using an unmanned aircraft [19,20] and satellites with spectral bands sensitive to agricultural variables [17,18].

To define the prediction variables of our estimation models, we used high-resolution multispectral images from the Planet satellite because our experiments were in small areas and there was a high availability of images referring to the crop development period.

Regarding the Planet satellite constellation, images were captured using a CCD camera equipped with a Bayer Mask filter. The sensor functions via photon filtering, and converts the photons into electrons. In this manner, the digital values of each pixel in each band are obtained through electron amplification. The Planet images have a spatial resolution of 3 m and a radiometric resolution that varies between 12 bits for the "analytic" images. The spectral resolution of the satellite consists of the following 4 bands: * spectral ranges (average wavelength) of blue ($\rho$485), green ($\rho$545), red ($\rho$630), and near-infrared ($\rho$820). Bands are captured with the Planet Scope 0, Planet Scope 1, and Planet Scope 2 optical instruments [21].

### *2.7. Processing of Multispectral Data*

The images from the Planet satellite can be obtained in the following three different processing levels: PlanetScope Basic Scene Product, PlanetScope Ortho Scene Product, and PlanetScene Ortho Tile Product. The variations between the supplied images oscillate between the presence of geometric correction (contained in the last two types of images) and the presence of the image in UTM projection (only the last image). In all cases, the supplied images are atmospherically corrected by the company; that is, the digital numbers of the bands are offered in surface reflectance values.

The images were obtained along the main phenological stages of corn development in the study area. In this phase, we only prioritized the images that presented significant spectral changes in the visible and near-infrared bands because there was little spectral variability in many of the consecutive stages. Note that each area has a distinct spectral characteristic where the spectral variability depends on abiotic and biotic factors of the culture and the date of cultivation.

The dates corresponding to the phenological stages of the study area are presented in Figure 3, which are indicated by green, whereas the red lines indicate the intervals at which the images were obtained.

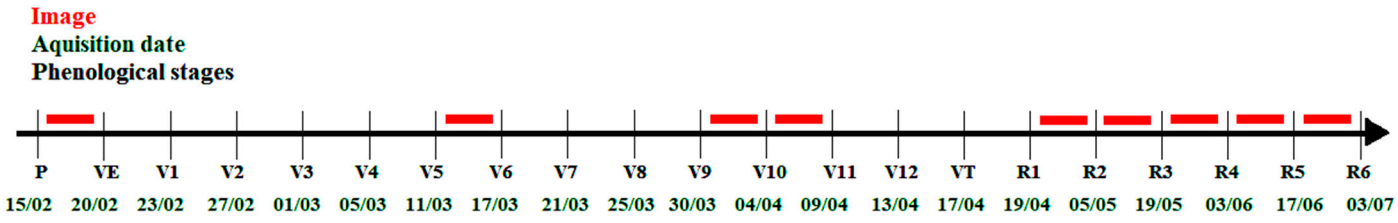


**Figure 3.** Corn crop, phenological stage V (vegetative), and reproductive (R) stage in image acquisition in the study area.

### *2.8. Calculation of Vegetation Indices*

Several studies have indicated that the multispectral vegetation indices comprise the spectral models of yield estimation [22,23]. The insertion of data of this nature makes the models more robust and assertive because the combination of bands in the indices highlights the vegetation characteristics, which are not detected with a single band [4].

In this study, we calculated the vegetation indices (Table 1) from the original Planet sensor bands. The calculation of the IR was conducted in the software ENVI 5.1. Note that the vegetation indices in Table 1 were selected because they highlight specific characteristics of the vegetation, such as biomass, vegetative vigor, pigmentation, and leaf area index.

**Table 1.** Equations and references for calculations of vegetation indices derived from original Planet satellite bands.

| Index | Equation | Reference | Contribution |
|---|---|---|---|
| Normalized difference vegetation index | $\frac{(\rho 820 - \rho 630)}{(\rho 820 + \rho 630)}$ | [24] | High correlation with yield |
| Green normalized difference | $\frac{(\rho 820 - \rho 545)}{(\rho 820 + \rho 545)}$ | [25] | Sensitivity to chlorophyll concentration |
| Ratio vegetation index | $\frac{\rho 630}{\rho 820}$ | [26,27] | Correlation with crop leaf density |
| Soil adjusted vegetation index | $\frac{(\rho 820 - \rho 630)}{(\rho 820 + \rho 630 + C) \times (1 + C)}$ | [28] | Minimizes the ground glare effect |
| Modified soil adjusted vegetation index [1] | $\frac{2 \times \rho 820 + 1 - \sqrt{d}}{2}$ | [29] | Minimizes the soil effect of the SAVI index |
| Optimized soil adjusted vegetation index | $\frac{(\rho 820 - \rho 630)}{(\rho 820 + \rho 630 + 0.16)}$ | [30] | Analysis on vegetative stages |
| Enhanced vegetation index | $\frac{\rho 545 \times (\rho 820 - \rho 630)}{(\rho 820 + C1 \times \rho 630 \times C2 \times \rho 485 + X)}$ | [31] | Enhance vegetation with less atmospheric influence |
| Triangular vegetation index | $\sqrt{NDVI + 0.5}$ | [32] | Sensitivity to crop leaf area index |
| Second modified triangular vegetation index | $\frac{1.5[2.5(\rho 820 - \rho 545) - 2.5(\rho 630 - \rho 545)]}{\sqrt{\left[(2 * \rho 820 + 1)^2 - 6 \times \rho 820 - 5 \times \sqrt{\rho 820} - 0.5\right]}}$ | [33] | Sensitivity to crop leaf area index |
| Chlorophyll vegetation index | $\frac{\rho 820 \times \rho 630}{\rho 545^2}$ | [34] | Increased sensitivity to chlorophyll |
| Chlorophyll index | $\frac{\rho 820}{\rho 545} - 1$ | [35] | Assists in estimating total plant chlorophyll |
| Green leaf index | $\frac{(2 \times \rho 545 - \rho 630 - \rho 485)}{(2 \times \rho 545 + \rho 630 + \rho 485)}$ | [36] | Leaf area intensity of the crop |
| Triangular greenness index | $-0.5[(\rho_{630} - \rho_{485})(\rho_{630} - \rho_{545}) - (\rho_{630} - \rho_{545})(\rho_{630} - \rho_{485})]$ | [28] | Enhances vegetation with low sensitivity to atmospheric effects |
| Normalized green, red difference index | $\frac{(\rho 545 - \rho 630)}{(\rho 545 + \rho 630)}$ | [37] | Correlation with crop biomass |

[1] $d = (2 \times \rho 820)2 - 8 \times (\rho 820 - \rho 630)$. $\rho$ refers to the satellite band and the number refers to the central wavelength of the spectral range. NDVI refers to normalized difference vegetation index. C refers to values as coefficients for atmospheric resistance. X refers to the value to be adjusted for canopy background.

### *2.9. Generation of Prediction and Quality Control Models*

For model generation, we selected samples from the total population of the yield data for each area. We divided each area into grids with 100 equal rectangles. The grids

were used to select one point per rectangle. Thus, a total of 100 points were selected from the entire data set, which was homogeneously distributed throughout each study plot (Figure 4). Points closest to the centroid of each rectangle were selected. The data points used for training and validation of the model were divided such that 80 points were randomly selected for model training and 20 points for validation.

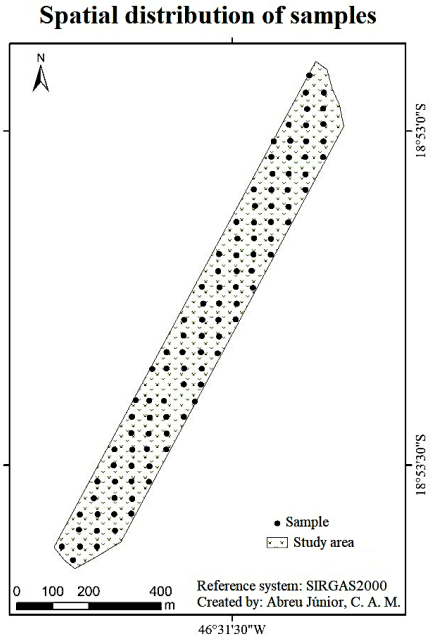


**Figure 4.** Spatial distribution of samples in the study areas.

The surface reflectance band values and the brightness of the multispectral indices were extracted by generating regions of interest using part of the points of the vectorial files. In this manner, each georeferenced yield value was related to the respective digital number in the image.

Following point selection, we calculated the yield and the spectral values derived from the images with the respective IVs using the Pearson model. Considering the high quantity of bands and IVs available to estimate yield, we defined criteria with a greater correlation with yield, for which the bands and vegetation indices would be predictor variables for each model.

We also justified this step of mining predictor variables as a strategy to mainly avoid overfitting of the generated models, which can occur when the number of parameters used in the regression is high. Thus, we selected the five highest absolute correlation values of the bands/IVs to develop the models. The indices/bands selected varied according to each phenological stage.

The following two types of methodologies were used to define the algorithms for yield estimation: (1) nonparametric regression methods, which included random trees (RTs), random forests (RFs), neural networks (NNs) and support vector machines (SVMs). It is important to emphasize that these algorithms were chosen by the application used in research to generate the spectral models for yield crop estimation. This step was developed in the Weka 3.9.5 software. RT, RF, NN, and SVM are learning techniques that use multiple decision trees. These are used to make a validation set from which statistical predictions are generated, which are based on sets of independent variables. Thus, it is easier to handle data from different sources, such as from images and field measurements, because the algorithm does not require for the data to present a normal statistical distribution. Due to this advantage, the algorithm has been widely used to resolve several agricultural problems, including estimating yield [12,38]. Table 2 presents the values of the input parameters in

the constitution of the non-parametric models for the two areas according to the default setting of the WEKA software (3.9).

**Table 2.** Input parameters for making support vector machine (A), neural net (B), and random forest (C) models in the study area for the research analyses. E.F. = Phenological stage; bS = batchSize; dNCC = doNotCheckCapabilities; fT = filterType; nDP = numDecimlPlaces; rO = regOptmizer; tT = trainingTime; hL = Hidden Layers; lR = learningRate; aB = autoBiuld; nTBF = nomialToBinaryFilter, nA = normalizeAtribute; nNC = normalizeNumericClass; tT = trainingTime; bSP = bagSizePercent; bTR = breakTiesRandomly; cOOB = calcOutOfBag; cAI = computeAttributeImportance, KV = KValue; aUI = allowUnclassifiedInstancess.

| **E.F.** | **Support Vector Machine** | | | | | | | |
|---|---|---|---|---|---|---|---|---|
| | bs | c | debug | dNCC | ft | kernel | nDP | rO |
| VE | 100 | 1.0 | False | False | Normalize | Polykernel | 2 | RegSMOImproved |
| R3 | 100 | 1.0 | False | False | Normalize | Polykernel | 2 | RegSMOImproved |

| **E.F.** | **Neural Net** | | | | | | | | |
|---|---|---|---|---|---|---|---|---|---|
| | GUI | aB | debug/decay/dNCC | bS | hL | IR | momentum | nTBF/nA/nNC | tT |
| V8 | False | True | False | 100 | 3 | 0.3 | 0.2 | True | 500 |
| V11 | False | True | False | 100 | 3 | 0.1 | 0.3 | True | 500 |
| R1 | False | True | False | 100 | 1 | 0.1 | 0.2 | True | 500 |
| R2 | False | True | False | 100 | 3 | 0.3 | 0.2 | True | 500 |

| **E.F.** | **Random Forest** | | | | | | | | |
|---|---|---|---|---|---|---|---|---|---|
| | bSP | bS | bTR | cOOB | Cai | debug | dNCC | maxDepth | Iterations |
| R5 | 100 | 100 | False | False | False | False | False | 0 | 100 |

| **E.F.** | **Random Tree** | | | | | | |
|---|---|---|---|---|---|---|---|
| | KV | allowUnclassified-Instancess | Bs | bTR/ dNCC | MaxDepth/ numFolds | minVarianceProp | minNum |
| V5 | 0 | False | 100 | False | 0 | 0.001 | 1.0 |
| R4 | 0 | False | 100 | False | 0 | 0.001 | 1.0 |
| R6 | 0 | False | 100 | False | 0 | 0.001 | 1.0 |

The mean absolute percentage error (*MAPE*%) (Equation (1)) and root mean square error percentage (*RMSE*%) were used for validation and analyses of the model accuracy as follows (Equation (2)):

$$MAPE(\%) = \frac{\frac{\sum_{i=1}^{n}|\hat{y}_i - y_i|}{y_i}}{n} \times 100 \quad (1)$$

where $\hat{y}_i$ is the predicted value, $y_i$ is the value observed in the field, and $n$ is the total number of elements.

$$RMSE\ (\%)\ = \frac{\sqrt{\frac{\sum_{i=1}^{n}(\hat{y}_i - y_i)^2}{n}} \times 100}{\sum_{i=1}^{n}\frac{y_i}{n}} \quad (2)$$

Here, $\hat{y}_i$ indicates the predicted values, $y_i$ are the values measured in the field, and $n$ is the total number of observations.

### *2.10. Map of the Discrepancy between Value Observed in the Field and Estimated by the Model*

Difference maps were created to analyze the results obtained via the estimation algorithms and to verify if there was a difference between the data observed in the field and those estimated by the models. Thus, it was possible to analyze whether the distribution generated by the model was primarily qualitative or quantitative, as well as determine the trends in space. We verified whether the model could record the low and high regions using this technique, regardless of the accuracy of the absolute values.

The maps were normalized with values ranging between −1 and 1. To complement the analysis, the evaluative metrics of RMSE and MAPE in this step, as well as the values of mean and standard deviation, which were derived from the map, were calculated once again. Thus, it was also possible to analyze the difference in the accuracy determined by the model and its application (the map).

## 3. Results

### *3.1. Exploratory Analysis of the Yield Variable*

Figure 5 presents the histogram of the study area for the yield variable, which is superimposed by a normal distribution curve (Table 3).

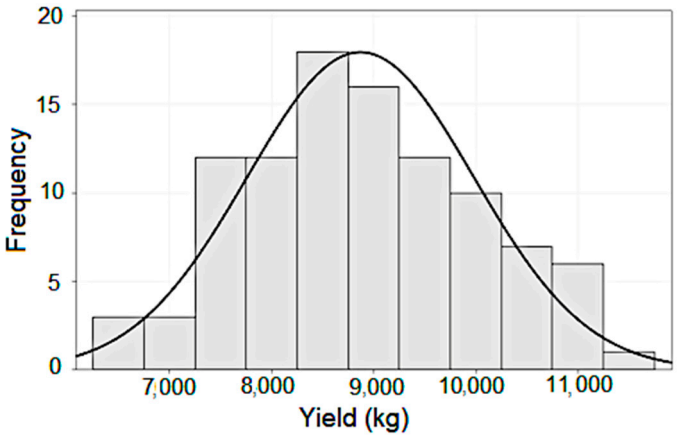


**Figure 5.** Histogram and normal distribution curve of the study area for the corn crop.

**Table 3.** Exploratory analysis of the yield variable: S.D. = standard deviation, Q1 = quartile 1, Q3 = quartile 3, C.V. = coefficient of variation.

| Variable | Average | D.P. | Minimum | Maximum | Q1 | Median | Q3 | C.V. (%) |
|---|---|---|---|---|---|---|---|---|
| Yield | 8871 | 1110 | 6345 | 11,254 | 8115 | 8808 | 9675 | 12.52 |

The upper and lower threshold values for the study area are 11,254 kg/ha and 6345 kg/ha, respectively. The first quartile (Q1) has a value of 8115 kg/ha, while the third quartile (Q3) has a value of 9675 kg/ha. Thus, 50% of the production values are comprised in the interval established between Q1 and Q3, which has an interquartile range of 1560 kg/ha. The average yield was equal to 8871 kg/ha, and is greater than the average yield of the state of Minas Gerais in the 2019/2020 harvest, which obtained a value of 5726 kg/ha [39]. The coefficient of variation (CV) was equal to 12.52%, which does not prevent the variable from being estimated. Ref. [40] managed to estimate the yield of the maize crop with significant results, despite having a CV value of 26.8% in vegetative stage 6.

### *3.2. Analysis of the Validation Metrics between Yield and Phenological Stages and Selection of the Best Model for Estimation*

Phenological stages and the validation metrics used, as well as the indices/flags that obtained the best response with the yield variable for each phenological stage are presented in Table 4.

**Table 4.** Analysis of the model performance according to phenological stage for the study area: neural network (NN), linear regression (LR), support vector machine (SVM), random forest (RF), algorithm (Alg.), root mean square error percentage (RMSE), and mean absolute percentage error (MAPE).

| Date | E.F. | Alg. | MAPE | RMSE | Bands/Indexes |
|---|---|---|---|---|---|
| 20//2002 | VE | SVM | 6.31 | 9.68 | GLI, VARI, GNDVI, CI-G, CVI |
| 13//2003 | V5 | RT | 7.09 | 9.62 | R, B, G, CVI, GNDVI |
| 31//2003 | V8 | NN | 7.39 | 9.70 | R, G, GNDVI, CI-G, CVI |
| 11//2004 | V11 | NN | 7.95 | 10.32 | CVI, CI-G, RVI, TGI, GNDVI |
| 25 April 2020 | R1 | NN | 7.25 | 9.25 | G. RVI, CVI, GNDVI, CI-G |
| 13//2005 | R2 | NN | 7.07 | 9.17 | NIR, CI-G, GNDVI, TVI, RVI |
| 22 May 2020 | R3 | SVM | 7.30 | 10.53 | EVI, CVI, NGRDI, VARI, TGI |
| 05//2006 | R4 | RT | 9.62 | 13.62 | G, GNDVI, CI-G, CVI, MTVI |
| 18//2006 | R5 | RF | 9.42 | 12.88 | NGRDI, VARI, TGI, EVI, RVI |
| 03//2007 | R6 | RT | 15.91 | 20.96 | MSAVI, MTVI, SAVI, OSAVI, NDVI |

The yield in the VE vegetative stage can be estimated with the RMSE and MAPE values for both areas, which were lower than 26% and 21%, respectively. The models are more assertive in R1 and VE, where the MAPE and RMSE values are lower than 25% and 23%, respectively.

Figure 6 also presents MAPE% and RMSE% trends, generated via the models of the yield estimation along the phenological stages.

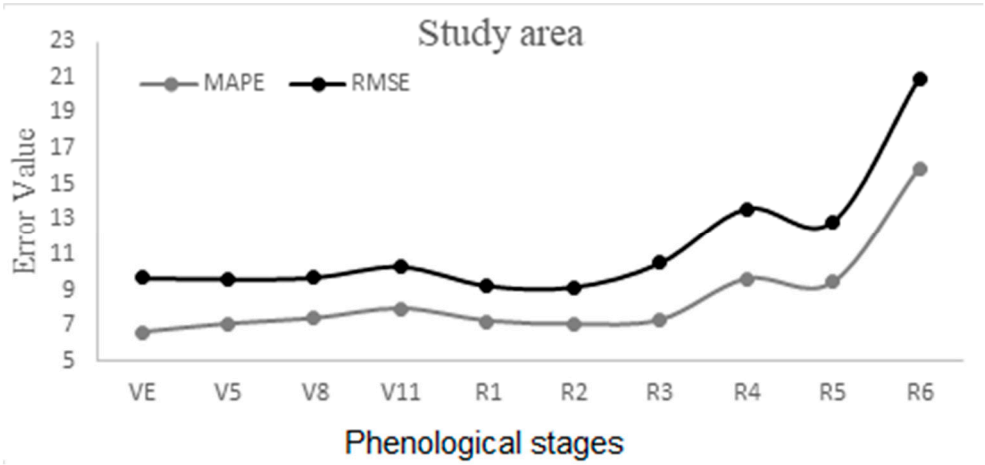


**Figure 6.** Root mean square error percentage (RMSE%) and mean absolute percentage error (MAPE%) curves for the study area.

The vegetative stage VE begins with a value near the lower threshold of the graph. Throughout the development of the base vegetative stages, there is a growth of values noted in V11. Hereon, a drop in the values of the metrics used is observed as the reproductive stages begin.

To better represent the variability between the observed and estimated yield values, the scatter plots of the observed versus estimated values for the study area are shown in Figure 7.

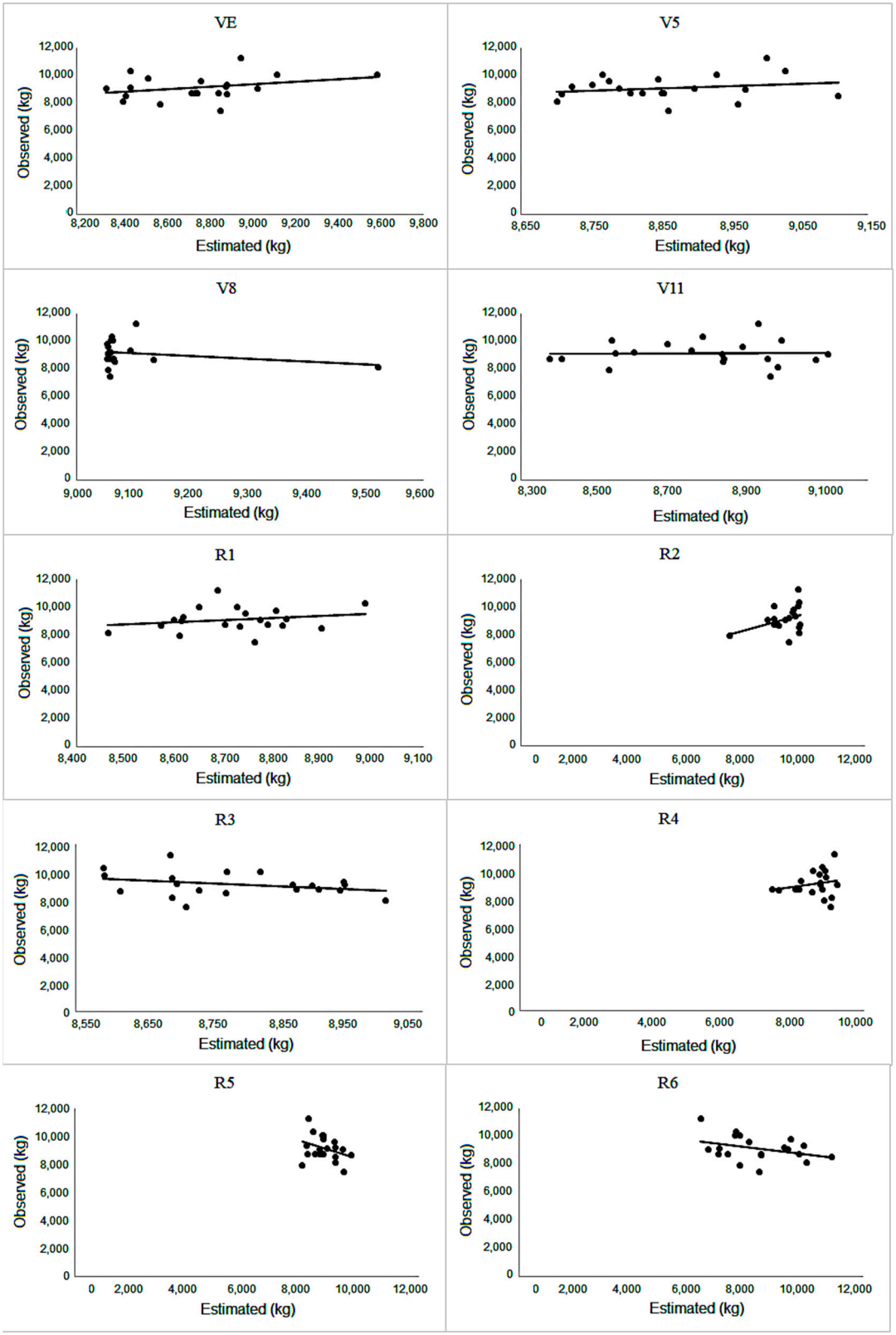


**Figure 7.** Observed x estimated values for the phenological stages of the study area.

The graphs in Figure 7 demonstrate the points associated with the estimated values, which are present in the ordinate axis, and the observed values, which are contained in the abscissa axis. For the VE, V5, V8, and V11 phenological stages, the data present a greater dispersion along the abscissa axis, following a linear trend. The data sets with the highest

angular coefficient are once again those with the highest deterministic coefficient, as shown in Table 4, which are in the VE, R2, R5, and R6 stages.

### *3.3. Spatialization of the Estimated Variable*

Results of the maps generated as a function of the yield estimate for Areas 1 and 2, are shown in (Figure 8A,B), respectively.

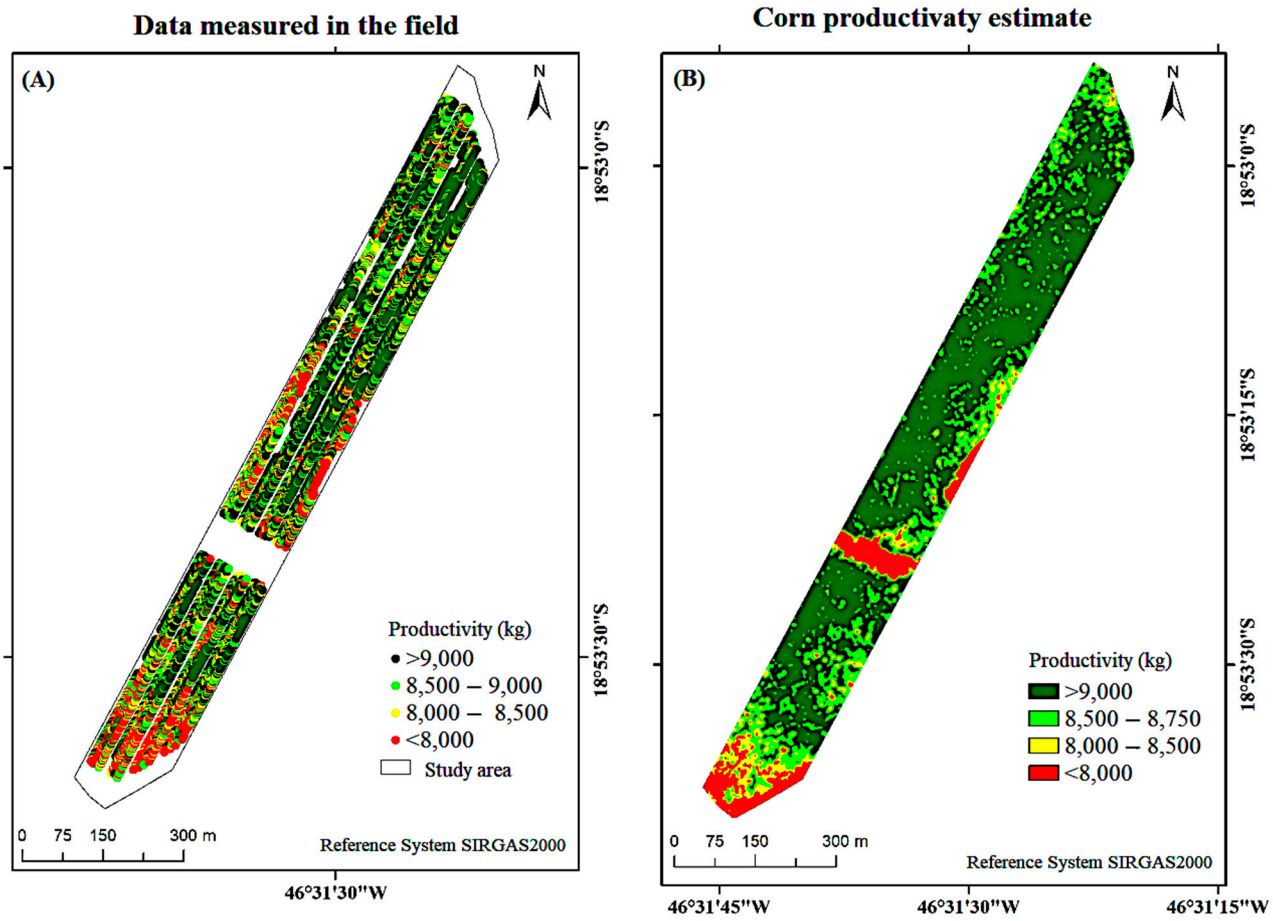


**Figure 8.** Spatial distribution of yield in the study area based on the data measured in the field (**A**) and spatial distribution of yield in the study area based on the SVM algorithm applied to the bands/indices (**B**) from the Planet satellite.

Points measured in the field (Figure 8A) and the result of the spatialization of the yield variable, which is calculated using the SVM model (Figure 8B) are shown. It is possible to identify the differences between the measured and estimated scenarios by analyzing the images. The primary difference is the number of values in the interval below 3000 kg, which is indicated in red. The second map presents a significant reduction in the area comprised in this interval. It is possible to verify the presence of vertical "lines" in both maps, which may be due to the difference of treatments used in the area.

Figure 9 presents the normalized difference between the estimated and observed values for each study area.

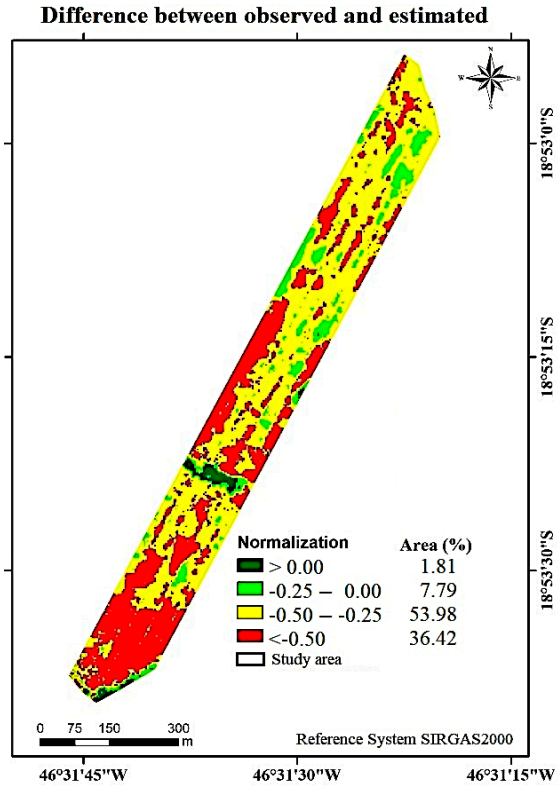


**Figure 9.** Difference between observed and estimated values.

The study area presents a greater difference in the lower portion of the plot and certain strips in the left and right extremities. The most significant proportion of values is located between the interval ranging from −0.5 to −0.25, with 53.98% of the areas centered in this class. These results corroborate those found in Table 5, although they are numerically different. In this context, the results are more quantitative and are closer to the values observed in the field.

**Table 5.** Statistics of observed and estimated surfaces indicating root mean square error percentage (RMSE) and mean absolute percentage error (MAPE).

| Metrics Analyzed | Study Area | |
|---|---|---|
| | Observed | Dear |
| Average | 9137.66 | 8448.98 |
| Standard Deviation | 924.62 | 917.76 |
| RMSE | 12.31 | |
| MAPE | 8.38 | |

## 4. Discussion

It is possible to observe the symmetrical trend of the data through a graphical analysis (Figure 5). This result corroborates with the smaller CV (Table 3) determined by the yield variable, thus indicating the potential of the variable to be estimated. However, a slight trend to the left of the graph is still noted, indicating inherent characteristics of a positive asymmetric curve.

In regard to the indices and bands used to create the spectral estimation and prediction models, the correlation analysis showed that the vegetation indices and bands do not fully explain the yield variation because there are many factors responsible for the final yield, but these indices can be useful as indicators of corn yield. Based on the RMSE%, MAPE% and R2 values obtained, spectral model performance reflects the possibility of remotely

estimating and predicting corn yield, despite the high spectral variability in the canopy caused by biotic and abiotic factors in the production environment.

Thus, the lowest values of MAPE% and RMSE% in the study area were found during R2, which indicates that R2 may be the ideal period for estimating yield in this phenological stage, where the plant is in the process of pollination. The stigma-styles were visible as they tried to capture the pollen grains [41]. The difference of 4 days indicates that the stigma-styles of each plant were already pollinated or in an advanced stage because this pollination period usually occurs between 2 and 3 days [42]. In a study [8], the authors tried to estimate the yield of the corn crop through multispectral images using the RNA Bayesian algorithm, where they determined that the best deterministic coefficient results for the generated estimation models are found 2 months before the harvest period, which may indicate a tendency for the estimation of yield in corn culture to present its apex before the harvest.

Overall, the results indicate that the algorithms with the highest incidence in the phenological stages were SVM, NN, and RT, which demonstrated a better performance in the phenological stages of VE and R3 for SVM; V8, V11, R1 and R2 for NN; V5, R4, and R6 for RT. The SVM algorithm is widely used in maize crops and demonstrates the ability to model different agronomic parameters, such as disease detection [43,44] and transpiration [45,46]. On the other hand, NN is used more frequently for yield estimation in maize crops, both through images obtained from remotely piloted aircrafts [47] and from orbital sensors [48]. To estimate yield through MODIS and GLASS satellite images, Wang et al. [48] used NN, which was based on a back-propagation algorithm. In the aforementioned study, the authors estimated yield with an MAPE value of less than 10%, and an RMSE at 700 kg/ha in most cases.

Based on the results in VE and V5, it is possible to observe the presence of visible bands, and the vegetation indices derived from them. The behavior of electromagnetic radiation in the visible range is mainly determined by chlorophyll. The mesophyll pigments tend to absorb wavelengths in the blue and red range [49]. Thus, the radiation from the green channel is reflected in a greater incidence, which may justify the presence of the green band and vegetation indices such as GNDVI and CI g in the models of the phenological stages of VE and V5. Based on the results in VE and V5, it is possible to observe the presence of visible bands, and vegetation 346 indices derived from them. The behavior of electromagnetic radiation in the visible range is mainly 347 determined by chlorophyll. The mesophyll pigments tend to absorb wavelengths in the blue and red range [49]. Thus, the radiation from the green channel is reflected in a greater incidence 349, which may justify the presence of the green band and the vegetation indices such as GNDVI and CI-G in the 350 models of the phenological stages of VE and V5.

The visible vegetation indices also comprise, in larger numbers, the models of the phenological stages of V8. In a study conducted by [48], the VARI and TGI indices presented the potential for estimating yield in corn crops; the authors generated models based on the NN algorithm, using six IV as the input parameters, among which were TGI and VARI.

The models arising from the phenological reproductive stages mark the presence of the near-infrared range for the first time among the input parameters used. It is possible to verify its presence in the R1, R2, R3, R4, R5, and R6 stages. The radiation coming from the near-infrared range tends to be sensitive to vegetation due to low absorption and backscattering when in contact with the internal cellular structures of the plant [49]. The reproductive stages mark the development of the corn ear [41].

In R1, the growth of the stalk and internodes are finalized. At this stage, the stigma-style continues its growth to be pollinated. Thus, the process of fertilization of the ovule can continue [42]. At R2, there is an accumulation of soluble sugars in the endosperm of the grain, which helps to increase the mass of grain. During this period, the corn ear is near the final fully developed size [41]. These internal changes may favor the greater reflectance from the near-infrared region and the vegetation indices derived from it.

The phenological stage of R6 is characterized by the physiological maturity of the grains. In this period, the senescence process in the leaves becomes more visible as they gain a "drier" appearance due to chlorophyll degradation. This stage is commonly destined to harvest once the grains are independent of the mother plant. In this context, the presence of the SAVI index and its variations of MSAVI and OSAVI, which are among those selected for the constitution of the R6 model, stand out.

The results displayed in Table 4 present an oscillation between the evaluation metrics used. In general, the possibility of estimating yield in the initial phenological stages is explained by the sensitivity of the bands and indices with macro and micronutrients of the exposed soil due to poorly developed crop canopy. Studies [50,51] have demonstrated that the amount of macro and micronutrients at the time of planting influence and have a high correlation with the final yield of the crop [52].

From the yield distribution maps, the treatments' effect were observed primarily in the corn plant trials in all sections of the study areas, where yield alternated according to natural crop development. The challenges in implementing the models in areas neighboring the study area require indexing of more yield data from other agricultural regions, that is, corn growing areas subject to different management techniques and environmental conditions. In relation to the spatial distribution pattern of yield classes, an irregular geometric pattern can be observed; that is, the map does not significantly reflect any spectral model sensitivity to the rectilinear geometry defined by the different irrigation sectors. Thus, the spatial distribution of yield is more conditioned to the biotic and abiotic factors of the crop itself; that is, the yield classes do not exhibit the influence of the anthropic actions applied in the experimental area.

## 5. Conclusions

The spectral yield estimation models show that the following:

- For estimating yield of the maize crop utilizing the spectral models based on multispectral images and machine learning algorithms, the reproductive phenological phase of R2 was found to obtain the best RMSE% and MAPE% values of 9.17% and 7.07%, respectively;
- Due to the influence of ground spectral response from images taken at the stadium
- VE, it is possible to estimate the yield with satisfactory levels of accuracy;
- The composition of the predictor variables and the accuracy and precision of the models are associated with the phenological stage of development; that is, the architecture of the model is variable for different areas and stages of senescence of the plant.

*Limitations and Future Perspectives*

A number of studies have been conducted to estimate corn yield using multispectral images. Similar to other studies presented in the literature, this study is limited to local prediction models, given that the data used are restricted to a planted area of 21.56 ha. The challenges in implementing the models in areas neighboring the study area require indexing of more yield data from other agricultural regions, that is, corn growing areas subject to different management techniques and environmental conditions.

From an economic standpoint, there is also a need to apply prediction models to multispectral sensors with better spatial resolutions. This is because the prediction models generated via images with average spatial resolution provide only general information of the real yield observed in loco. Corn is one of the most valuable agricultural crops in the world, and thus, the more specific the information, the more justifiable is the implementation of this technology for crop management.

**Author Contributions:** Conceptualization, C.A.M.d.A.J. and G.D.M.; methodology, C.A.M.d.A.J.; validation, G.D.M.; J.V.M.B., D.J.M. and G.d.O.; formal analysis, G.D.M.; J.V.M.B., D.J.M. and G.d.O.; investigation, L.C.M.X.; resources, C.A.M.d.A.J.; data curation, L.C.M.X.; writing—original draft preparation, C.A.M.d.A.J.; writing—review and editing, L.C.M.X.; visualization, L.C.M.X.; supervision, G.D.M., J.V.M.B., D.J.M. and G.d.O.; project administration, G.D.M.; funding acquisition, G.d.O. All authors have read and agreed to the published version of the manuscript.

**Funding:** The research was financed by the company Lallemand Plant Care, through a partnership with the Federal University of Uberlândia, Brazil for the promotion of student grants for the development of research.

**Data Availability Statement:** The datasets generated during and/or analyzed during the present study are not publicly available since, despite being anonymized, they portray a single farm, so publicly sharing the data can be experienced as sensitive for the case study participants. Datasets are available from the corresponding author on reasonable request.

**Acknowledgments:** We thank the Universidade Federal de Uberlândia for the assistance and training provided to the authors. The company Lallemand Plant Care for the support and supply of the data used in this research.

**Conflicts of Interest:** The authors declare no conflict of interest.

## References

1. Terliksiz, A.S.; Altýlar, D.T. Use of deep neural networks for crop yield prediction: A case study of soybean yield in Lauderdale County, Alabama, USA. In Proceedings of the 8th International Conference on Agro654 Geoinformatics (Agro-Geoinformatics), Istanbul, Turkey, 16 July 2019.
2. Filgueiras, R.; Almeida, T.S.; Mantovani, E.C.; Dias, S.H.B.; Fernandes-Filho, E.I.; da Cunha, F.F.; Venancio, L.P. Soil water content and actual evapotranspiration predictions using regression algorithms and remote sensing data. *Agric. Water Manag.* **2020**, *241*, 106346. [CrossRef]
3. Shanahan, J.; Dennis, D.; Francis, G.E.; Wallace, W.V.; Wilhelm, W.; Tringe, J.W.; Schlemmer, M.R.; Major, D.J. Use of Remote-Sensing Imagery to Estimate Corn Grain Yield. *Agron. J.* **2001**, *93*, 583–589. [CrossRef]
4. Jensen, J. *Remote Sensing of the Environment: An Earth Resource Perspective*, 2nd ed.; Pearson PrenticeHall: Upper Saddle River, NJ, USA, 2009; 525p.
5. Eugenio, F.C.; Grohs, M.; Venancio, L.P.; Schuh, M.; Bottega, E.L.; Ruoso, R.; Schons, C.; Lorenci Mallman, C.; Badin, T.L.; Fernandes, P. Estimation of soybean yield from machine learning techniques and multispectral RPAS imagery. *Remote Sens. Appl. Soc. Environ.* **2020**, *27*, 100782. [CrossRef]
6. Barzin, R.; Pathak, R.; Lotfi, H.; Varco, J.; Bora, G.C. Use of UAS multispectral imagery at different physiological stages for yield prediction and input resource optimization in corn. *Remote Sens.* **2020**, *12*, 2392. [CrossRef]
7. Ješovnik, A.; Blažević, I.; Lemić, D.; Pajač Živković, I. Ant fauna of annual and perennial crops. *Appl. Ecol. Environ. Res.* **2019**, *17*, 12709–12722. [CrossRef]
8. Ma, Y.; Zhang, Z.; Kang, Y.; Mutlu Özdoğan, M. Corn yield prediction and uncertainty analysis based on remotely sensed variables using a Bayesian neural network approach. *Remote Sens. Environ.* **2021**, *259*, 112408. [CrossRef]
9. Ahmad, I.; Saeed, U.; Fahad, M.; Ullah, A.; Rahman, M.H.; Ahmad, A.; Judge, J. Yield forecasting of spring maize using remote sensing and crop modeling in Faisalabad-Punjab Pakistan. *J. Indian Soc. Remote Sens.* **2018**, *46*, 1701–1711. [CrossRef]
10. Wahab, I.; Hall, O.; Jirström, M. Remote sensing of yields: Application of UAV imagery-derived NDVI for estimating maize vigor and yields in complex farming systems in Sub-Saharan Africa. *Drones* **2018**, *2*, 28. [CrossRef]
11. Khaki, S.; Pham, H.; Wang, L. Simultaneous corn and soybean yield prediction from remote sensing data using deep transfer learning. *Sci. Rep.* **2021**, *11*, 11132. [CrossRef]
12. Khanal, S.; Klopfenstein, A.; Ramarao, V.V.; Ramarao, J.F.; Fulton, J.; Nathan, D.; Scott, A.; Shearer, S. Assessing the impact of agricultural field traffic on corn grain yield using remote sensing and machine learning. *Soil Tillage Res.* **2021**, *208*, 104880. [CrossRef]
13. Tandzi, N.L.; Mutengwa, S.M. Estimation of maize (*Zea mays* L.) yield per harvest area: Appropriate methods. *Agronomy* **2020**, *10*, 29. [CrossRef]
14. Soybean and Corn Cultivation Systems in the Alto Paranaíba-MG Region and Evaluation Results in the 2014/15 Harvest. Available online: https://ainfo.cnptia.embrapa.br/digital/bitstream/item/149709/1/doc-200 (accessed on 1 July 2022).
15. Baum, M.E.; Archontoulis, S.V.; Licht, M.A. Planting date, hybrid maturity, and weather effects on maize yield and crop stage. *Agron. J.* **2019**, *111*, 303–313. [CrossRef]
16. Oliveira, A.; Mello, C.; Marques, R. Temporal trends of climate indices associated with precipitation and air temperature in Minas Gerais, Brazil. *Rev. Bras. Climatol.* **2020**, *26*, 499–520. [CrossRef]
17. Ji, Z.; Pan, Z.; Zhu, X.; Wang, J.; Li, Q. Prediction of Crop Yield Using Phenological Information Extracted from Remote Sensing Vegetation Index. *Sensors* **2021**, *21*, 1406. [CrossRef] [PubMed]

18. Jie Sun, J.; Lai, Z.; Di, L.; Sun, Z.; Tao, J.; Shen, Y. Multilevel deep learning network for county-level corn yield estimation in the u.s. corn belt. *IEEE J. Sel. Top. Appl. Earth Obs. Remote Sens.* **2020**, *13*, 5048–5060. [CrossRef]
19. Guo, Y.; Wang, H.; Wu, Z.; Wang, S.; Sun, H.; Senthilnath, J.; Wang, J.; Bryant, C.; Fu, Y. Modified red blue vegetation index for chlorophyll estimation and yield prediction of maize from visible images captured by UAV. *Sensors* **2020**, *20*, 5055. [CrossRef] [PubMed]
20. Fathipoor, H.; Arefi, H.; Shah-Hosseini, R.; Moghadam, H. Corn forage yield prediction using unmanned aerial vehicle images at mid-season growth stage. *J. Appl. Remote Sens.* **2019**, *13*, 034503. [CrossRef]
21. Planet Labs Specifications: Spacecraft Operations & Ground Systems. Planet Labs. Available online: https://docplayer.net/45671690-Planet-labs-specifications-spacecraft-operations-ground-systems-1-section-header-planet-labs-spacecraft-operations-ground-systems.html (accessed on 1 July 2022).
22. Marques Ramos, A.P.; Prado Osco, L.; Furuya, D.E.G.; Gonçalves, W.N.; Santana, D.C.; Teodoro, L.P.; da Silva Junior, C.A.; Capristo-Silva, G.F.; Li, J.; Rojo Baio, F.H.; et al. A random forest ranking approach to predict yield in maize with uav-based vegetation spectral indices. *Comput. Electron. Agric.* **2020**, *178*, 105791. [CrossRef]
23. Aghighi, H.; Azadbakht, M.; Ashourloo, D.; Shahrabi, H.S.; Radiom, S. Machine learning regression techniques for the silage maize yield prediction using time-series images of landsat 8 OLI. *IEEE J. Sel. Top. Appl. Earth Obs. Remote Sens.* **2018**, *11*, 4563–4577. [CrossRef]
24. Monitoring Vegetation Systems in the Great Plains with ERTS, NASA Special Publication. 1974. Available online: https://ntrs.nasa.gov/citations/19740022614 (accessed on 1 July 2022).
25. Gitelson, A.A.; Kaufman, Y.J.; Merzlyak, M.N. Use of a green channel in remote sensing of global vegetation from EOS-MODIS. *Remote Sens. Environ.* **1996**, *58*, 289–298. [CrossRef]
26. Jordan, C.F. Derivation of leaf area index from quality of light on the forest floor. *Ecology* **1969**, *50*, 663–666. [CrossRef]
27. Pearson, R.L.; Miller, L.D. U.S. Remote mapping of standing crop biomass for estimation of the yield of the shortgrass prairie, Pawnee National Grasslands, Colorado. In Proceedings of the International Symposium on Remote Sensing of Environment, Pawnee National Grasslands, CO, USA, 2–6 October 1972.
28. Hunt, E.R.; Daughtry, C.S.T.; Eitel, J.U.H.; Long, D.S. Remote sensing leaf chlorophyll content using a visible band index. *Agron. J.* **2011**, *103*, 1090. [CrossRef]
29. Qi, J.; Chehbouni, A.; Huete, A.R.; Kerr, Y.H.; Sorooshian, S. A modified soil adjusted vegetation index. *Remote Sens. Environ.* **1994**, *48*, 119–126. [CrossRef]
30. Rondeaux, G.; Steven, M.; Baret, F. Optimization of soil-adjusted vegetation indices. *Remote Sens. Environ.* **1996**, *55*, 95–107. [CrossRef]
31. Huete, A.; Didan, K.; Miura, T.E.; Rodrigueza, P.; Gaoa, X.; Ferreirab, L.G. Overview of the radiometric and biophysical performance of the MODIS vegetation indices. *Remote Sens. Environ.* **2002**, *83*, 195–213. [CrossRef]
32. Broge, N.H.; Leblanc, E. Comparing predictive power and stability of broadband and hyperspectral vegetation indices for estimation of green leaf area index and canopy chlorophyll density. *Remote Sens. Environ.* **2000**, *76*, 156–172. [CrossRef]
33. Haboudane, D.; Miller, J.R.; Pattey, E.; Zarco-Tejada, P.J.; Strachan, I.B. Hyperspectral vegetation indices and novel algorithms for predicting green LAI of crop canopies: Modeling and validation in the context of precision agriculture. *Remote Sens. Environ.* **2004**, *90*, 337–352. [CrossRef]
34. Vincini, M.; Frazzi, E.; D'Alessio, P. A broad-band leaf chlorophyll index at the canopy scale. *Precis. Agric.* **2008**, *9*, 303–319. [CrossRef]
35. Gitelson, A.A.; Gritz, Y.; Merzlyak, M.N. Relationships between leaf chlorophyll content and spectral reflectance and algorithms for nondestructive chlorophyll assessment in higher plant leaves. *J. Plant Physiol.* **2003**, *160*, 271–278. [CrossRef]
36. Louhaichi, M.; Borman, M.M.; Johnson, D.E. Spatially located platform and aerial photography for documentation of grazing impacts on wheat. *Geocarto Int.* **2001**, *16*, 1. [CrossRef]
37. Tucker, C.J. Red and photographic infrared linear combinations for monitoring vegetation. *Remote Sens. Environ.* **1979**, *8*, 127–150. [CrossRef]
38. Arab, S.T.; Noguchi, R.; Matsushita, S.; Ahamed, T. Prediction of grape yields from time-series vegetation indices using satellite remote sensing and a machine-learning approach. *Remote Sens. Appl. Soc. Environ.* **2021**, *22*, 100485. [CrossRef]
39. Accompaniment of the Brazilian Grain Crop: Twelfth Survey. Available online: https://www.conab.gov.br/infoagro/safras/gr%C3%A3os (accessed on 1 July 2022).
40. Tagarakis, A.; Ketterings, Q. In-season estimation of corn yield potential using proximal sensing. *Agron. J.* **2017**, *109*, 1323–1330. [CrossRef]
41. Corn: Brazil Expands Cultivation to Meet Growing Demand. Available online: https://www.esalq.usp.br/visaoagricola/sites/default/files/Esalq-VA13-Milho.pdf (accessed on 1 July 2022).
42. Physiology of Corn Production, Technical Circular, Infoteca-e. Available online: http://www.infoteca.cnptia.embrapa.br/infoteca/handle/doc/490408 (accessed on 1 July 2022).
43. Alehegn, E. Ethiopian maize diseases recognition and classification using support vector machine. *Int. J. Comput. Vis. Robot.* **2019**, *9*, 90–109. [CrossRef]

44. Aravind, K.R.; Raja, P.; Aniirudh, R.; Ashiwin, R. Disease classification in maize crop using bag of features and multiclass support vector machine. In Proceedings of the Second International Conference on Inventive Systems and Control, Piscataway, NJ, USA, 19 January 2018.
45. Fan, J.; Zheng, J.; Wu, L.; Zhang, F. Estimation of daily maize transpiration using support vector machines, extreme gradient boosting, artificial and deep neural networks models. *Agric. Water Manag.* **2021**, *245*, 106547. [CrossRef]
46. Zheng, J.; Fan, J.; Zhang, F.; Wud, L.; Zoua, Y.; Zhuangbc, Q. Estimation of rainfed maize transpiration under various mulching methods using modified Jarvis-Stewart model and hybrid support vector machine model with whale optimization algorithm. *Agric. Water Manag.* **2021**, *249*, 106799. [CrossRef]
47. García-Martínez, H.; Flores-Magdaleno, H.; Ascencio-Hernández, R.; Khalil-Gardezi, A.; Tijerina-Chávez, L.; Mancilla-Villa, O.R.; Vázquez-Peña, M.A. Corn Grain Yield Estimation from Vegetation Indices, Canopy Cover, Plant Density, and a Neural Network Using Multispectral and RGB Images Acquired with Unmanned Aerial Vehicles. *Agriculture* **2020**, *10*, 277. [CrossRef]
48. Wang, L.; Wang, P.; Liang, S.; Yongchao, Z.; Khan, J.; Shibo Fang, S. Monitoring maize growth on the North China Plain using a hybrid genetic algorithm-based back-propagation neural network model. *Comput. Electron. Agric.* **2020**, *170*, 105238. [CrossRef]
49. Liesenberg, V.; Galvão, L.S.; Ponzoni, F.J. Variations in reflectance with seasonality and viewing geometry: Implications for classification of Brazilian savanna physiognomies with MISR/Terra data. *Remote Sens. Environ.* **2007**, *107*, 276–286. [CrossRef]
50. Ray, K.; Banerjee, H.; Dutta, S.; Hazra, A.K.; Majumdar, K. Macronutrients influence yield and oil quality of hybrid maize (*Zea mays* L.). *PLoS ONE* **2019**, *14*, e0216939. [CrossRef]
51. Babu, S.; Singh, R.; Avasthe, R.K.; Yadav, G.S.; Das, A.; Singh, V.K.; Mohapatra, K.P.; Rathore, S.S.; Chandra, P.; Kumar, A. Impact of land configuration and organic nutrient management on yield, quality and soil properties under baby corn in Eastern Himalayas. *Sci. Rep.* **2020**, *10*, 16129. [CrossRef] [PubMed]
52. Selvi, K.C.; Coskun, G.; Mehmet, A.B. Short Term Effects of Different Tillage Methods on Nitrate Content in Soil and Corn Yield. *Malays. J. Soil Sci.* **2019**, *23*, 55–68.


**Disclaimer/Publisher's Note:** The statements, opinions and data contained in all publications are solely those of the individual author(s) and contributor(s) and not of MDPI and/or the editor(s). MDPI and/or the editor(s) disclaim responsibility for any injury to people or property resulting from any ideas, methods, instructions or products referred to in the content.